Electron microscopy study of the formation mechanism of catalytic nickel rich particles and the role of carbonyl sulphide in the suppression of carbon deposition on 20Cr-25Ni steel

Rai, Subash; Taylor, Mary; Chiu, Yu-Lung; Evans, Hugh; Connolly, Brian; Smith, Neal; Mowforth, Clive

DOI:
10.1016/j.matchar.2018.07.039

Accepted Manuscript

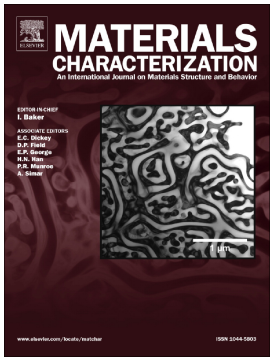

Electron microscopy study of the formation mechanism of catalytic nickel-rich particles and the role of carbonyl sulphide in the suppression of carbon deposition on 20Cr-25Ni steel

S. Rai, M.P. Taylor, Y.L. Chiu, H.E. Evans, B.J. Connolly, N. Smith, C.W. Mowforth

PII:	S1044-5803(18)31273-7
DOI:	doi:10.1016/j.matchar.2018.07.039
Reference:	MTL 9331
To appear in:	*Materials Characterization*
Received date:	2 May 2018
Revised date:	31 July 2018
Accepted date:	31 July 2018

Please cite this article as: S. Rai, M.P. Taylor, Y.L. Chiu, H.E. Evans, B.J. Connolly, N. Smith, C.W. Mowforth , Electron microscopy study of the formation mechanism of catalytic nickel-rich particles and the role of carbonyl sulphide in the suppression of carbon deposition on 20Cr-25Ni steel. Mtl (2018), doi:10.1016/j.matchar.2018.07.039

Electron microscopy study of the formation mechanism of catalytic nickel-rich particles and the role of carbonyl sulphide in the suppression of carbon deposition on 20Cr-25Ni steel

S. Rai[1], M. P. Taylor[1], Y. L. Chiu[1*], H. E. Evans[1], B. J. Connolly[1,2], N. Smith[3] and C. W. Mowforth[3]

[1]School of Metallurgy and Materials, University of Birmingham, Birmingham, B15 2TT, UK

[2]University of Manchester, Manchester, M13 9PL, UK

[3]EDF Energy, Barnwood, Gloucester, GL4 3RS, UK

Abstract: Austenitic stainless steel is used as fuel cladding in advanced gas-cooled nuclear reactors (AGR). At elevated temperatures, when the steel is exposed to CO_2 based environments filamentary carbon deposits form on the surface of the steel. This filamentary carbon deposition is known to be catalysed by metallic nickel-rich particles. Adding trace amount of carbonyl sulphide (COS) into the gas mixtures suppresses the carbon deposition. In this current work, it has been shown that at 600 °C, the formation of filamentary carbon was suppressed by the addition of 215 ppb COS to a depositing gas mixture (containing approximately 1000 vppm C_2H_4 / 1% CO / bal. CO_2) which was known to provide the environment suitable for carbon deposition. Samples exposed to the gas mixtures with and without 215 ppb COS were characterised using electron microscopy techniques to understand the formation mechanism of the nickel-rich particles and the inhibition mechanism due to the addition of COS. Electron diffraction study shows that the nickel-rich particles in the oxide layers assume the same crystallography as that of the austenitic metal underneath, regardless of the COS addition. The current observations also show that the metal-oxide interfaces was nickel-rich and a simple model has been proposed to explain the formation of nickel-rich particles within the subsurface oxide. Furthermore, it was found that when COS was added the surface of the nickel-rich particles in the oxide layer was found to be sulphur-rich by energy dispersive spectroscopy (EDS) on a scanning transmission electron microscope (STEM). It is believed that the surface sulphur adsorption onto the nickel-rich particles, rather than bulk sulphide formation, resulted in the inhibition of carbon deformation on the steel.

KEYWORDS: Carbon deposition; Catalyst Poisoning; Sulphur Adsorption; STEM-EDS; Electron Diffraction.

*Corresponding Author. Email: y.chiu@bham.ac.uk (Y. L. Chiu)

1. Introduction

Austenitic steel has been used for many high-temperature applications which require good heat conductivity and mechanical stability. For instance, austenitic steel containing about 20 wt.% chromium and 25 wt.% nickel (20Cr-25Ni) has been used as the fuel cladding in Advanced Gas-cooled Reactors (AGR) which use CO/CO_2 as a coolant. The deposition of carbon on the surface of the 20Cr-25Ni steel occurs at its operating temperatures in the reactor [1]. The excessive accumulation of such carbon deposits impairs the heat transfer efficiency [2]. Hence, it is of both technological and economic interest to inhibit the carbon deposition on the cladding steel. When exposed to a gas mixture with carbon activity greater than unity at 550°C, it has been shown that the deposited carbon filaments on 20Cr-25Ni steel were catalysed by metallic nickel particles [3]. Since there was no other external nickel source in the experiment, it was postulated that the nickel particles that catalysed the carbon deposition originated from the 20Cr-25Ni steel. It has also been reported that catalytic austenitic [4] and nickel particles [5], identified within coke, were formed by metal disintegration during the metal dusting phenomena. However these observations reported [4-5] were mainly on highly reducing gaseous environment unlike in the current work where oxidation of alloy leads to the formation of the nickel-rich particles, as reported earlier [3, 6]. These nickel-rich particles will be carefully characterise to understand their formation mechanism.

One way to suppress the carbon deposition on the cladding steel is to form a physical barrier such as the protective chromia [3] and/or silica layers [3, 7] or to increase the oxygen potential of the system such that the oxidation of nickel is favourable [6]. Due to practical reasons, the most extensively studied method to inhibit the carbon deposition, however, is to alter the chemistry of the catalyst by introducing sulphur-containing compound [8, 9, 10, 11, 12]. Recently, the effect of carbonyl sulphide (COS) on carbon deposition was studied over the temperature range 500-725°C [13]. It was shown that the concentration of COS necessary to inhibit carbon deposition process increases with temperature. Two possible mechanisms [14] have been proposed on the role of sulphur in deactivating nickel particles, namely bulk sulphiding and surface poisoning by sulphur adsorption. No experimental evidence supporting either mechanism has been obtained previously [14]. The previous study relied on characterisation techniques such as scanning electron microscopy (SEM) which

however was not able to analyse the chemical information of the individual nickel particles due to their small sizes. Using a combination of focused ion beam (FIB) sample preparation and detailed transmission electron microscopy characterisation, this project aims to study the formation mechanism of the catalytic nickel-rich particles and to improve the understanding of the inhibiting role of carbonyl sulphide (COS) on the carbon deposition on 20Cr-25Ni steel.

2. Experimental Procedure

The steel used in this work was a cold-rolled strip with a thickness of 0.4 mm and the composition given in Table 1. Samples with dimensions of approximately 10 mm x 20 mm x 0.4 mm were ground down to 0.3 mm thickness using wet silicon carbide paper progressively from 240 to 1200 grit, followed by successive mechanical polishing with 6 µm and 1 µm diamond paste and final finishing using colloidal silica of 0.04 µm. The samples were wrapped in tantalum foil and annealed at 930 °C in Ar gas containing 5% H_2 for 30 min to achieve a uniform final grain size of approximately 13 µm. Along with these rectangular samples, discs 3 mm diameter were also prepared for TEM observations. The discs were annealed following the same condition as described above and then twin-jet electro-polished in an electrolyte containing 10% perchloric acid and 90% ethanol at -5°C to -20°C and 12 V. The polished discs were thoroughly cleaned with ethanol and were later used for carbon deposition and then TEM observations.

As illustrated in Figure 1, the test rig system used for this study consisted of two horizontal tube furnaces connected in series and connected with two gas bottles, one was an inert gas containing 5% hydrogen in argon and the other was a bottle containing the deposition gas mixture. The specimens were placed in an alumina boat and transferred to the central region of the treatment furnace. Clean titanium foil was placed in the pre-treatment furnace, used here as an oxygen getter. The inert gas was used to purge through the rig for 2 hours. The pre-treatment furnace was heated up to 700 °C at 20 °C per minute and maintained at this temperature for 20 minutes. While maintaining the inert gas flow, the treatment furnace was heated up at 20°C per minute to 600 °C and maintained for 30 minutes. The Ar gas (containing 5% H_2) flow was stopped and the selected deposition gas mixture bottle was

switched on. After 4 hours deposition experiment, the treatment furnace was switched off and the gas supply was switched back to the inert gas. Two hours later the pre-treatment furnace was also switched off, and the rig was allowed to cool overnight to room temperature under the flowing inert gas. The sample was then removed from the furnace for analysis. During the experiment, the inert gas flow rate was maintained at 0.5 L/min and the deposition gas at 1 L/min. The test was conducted at atmospheric pressure.

Pre-mixed gas bottles were supplied by BOC with the certified composition shown in Table 2. The high carbon activity ($a_c > 1$) needed for carbon deposition arises from the dissociation of ethene (C_2H_4) and it is expected to be in the range of $10^2 < a_c < 10^7$ [3, 6]. The oxygen activity is controlled by the ratio of CO/CO_2 and is estimated to be approximately 10^{-23} at 600 ^oC in both gas mixtures. At this oxygen activity, both iron and chromium are expected to be oxidised but not nickel [3, 6].

In order to analyse the details of the nickel-rich particles embedded in the oxide layers, thin foils were prepared from the bulk sample using an FEI Quanta 3D FEG FIB/SEM. Composition maps were acquired from the surface and the cross-sectional samples on a TESCAN MIRA 3 SEM associated with an X-max SDD detector and a TALOS F200X STEM associated with a Super-X EDS system which is characterised by its four windowless silicon drift detectors with the total detection area of 120 mm^2 and solid angle of 0.9 str. TEM imaging and nano-beam electron diffraction (NBED) analysis of individual particles were carried out using a JEOL-2100 TEM. Both Talos F200X and JEOL-2100 were operated at 200 kV.

3. Results

3.1. Sulphur-free carbon deposition

Figure 2a shows the typical surface structure of the sample following the test in the sulphur-free gas mixture. The surface was covered with carbon deposits which were filamentary in nature as seen in the inset. The distribution of carbon and iron on the surface of the sample is shown by the EDS elemental maps in Figures 2b and 2c. It clearly demonstrates that the deposition was concentrated at

the grain centres. In Figure 2, the grain boundaries were outlines by the yellow dashed lines. This lower carbon deposition at grain boundaries (g.b.) was probably provided by the protective chromia layer [3, 13], which preferentially forms at grain boundaries [15] during the early stage of oxidation, due to the fast diffusion of chromium via these paths to the surface of the alloy. Adjacent to the grain boundaries, long and continuous particles of a few micrometers in size were observed. EDS analysis showed that these particles were iron-rich (Figure 2c). Although the formation of metallic Fe particles under 1% CO/CO_2 is thermodynamically unfavourable [3], it is possible that the iron-rich particles were formed via a reduction reaction occurring during the cooling stage under the 5% hydrogen in argon. Further studies will be needed to clarify this though.

At high magnification, it was observed that the carbon filaments consisted of a bright particle at their tips (Figure 2a, inset). The nature of the particle was studied using TEM. Figures 3a and 3b show carbon filaments projecting from the edge of a 3 mm diameter TEM disc exposed in the sulphur-free deposition gas mixture for 4 hours at 600 °C. The high angle annular dark field (HAADF) image and the EDS maps obtained (Figures 3(b-e)) showed that the particles were composed of nickel and iron and connected to the sample edge by thin carbon filaments.

The size and composition of these particles were measured. As shown in Figure 3f the particle sizes ranged from 5 to 120 nm with an average of 58 nm. EDS spectra were collected only from those particles located at the tip of filaments projecting from the edge of the sample, in order to minimise the effect of the bulk alloy. The chemical composition determination was based on the assumption that the particles of 50 nm thick were involved without the accurate measurement of sample thicknesses in each measurement. It has been noticed that while the thickness of the particle varied from 10 nm to 150 nm in the calculation, the nickel concentration measured varies within 0.1 at%. Therefore assuming the thickness of 50 nm is not expected to have a significant impact on the results obtained. Each spectrum was recorded for a 20 seconds dwell time which typically collected over 200,000 counts of X-ray photons. Figure 3g shows that the nickel-iron ratios measured from most particles are larger than 4 (in the range of 2.9 to 11.2, with an average of 5). This result agrees well with the work of Park and Baker [16] who investigated the decomposition of ethylene over nickel-iron

bimetallic particle to produce methane, ethane and solid carbon (identified as filamentous in nature). They observed that the conversion of ethylene over nickel-iron particles with nickel content of 70% or less is extremely low. However, there was a dramatic increase in the conversion of ethylene into solid carbon when nickel concentration was greater than 75%.

Figure 4a shows a nickel-rich particle on the same sample. The electron diffraction patterns obtained (as shown for example in Figure 4b) is consistent with the face-centred cubic (FCC) structure with the lattice parameter of about 3.6 Å. The high-resolution image in Figure 4c shows the turbostratic structure of the carbon encapsulating a nickel-rich particle. The lattice fringes of the particle are clearly visible. The measured fringe spacing was approximately 0.2 nm, close to {111} inter-planar spacing of FCC nickel. These observations are consistent with a previous study [3].

3.2. Effect of 215 ppb COS on carbon deposition

After the exposure in the gas mixture containing 215 ppb COS, no carbon filaments were observed on the sample using an SEM. Figure 5a is an SEM micrograph showing the surface of the sample after the test. The EDS map of carbon (Figure 5b) shows only a very small amount of carbon present on the surface. The grain centres were decorated with light contrast particles which were found to be nickel- and iron-rich (Figure 5c). Some of these particles were held together into clusters by non-filamentary carbon (marked as NFC in the image), consistent with the elemental carbon map. Larger micrometre-sized iron-rich particles, as described earlier, were also present. Figure 5d shows the carbon X-ray peaks collected from the sample exposed in the sulphur-free gas mixture and that in the mixture containing 215 ppb COS, under otherwise identical conditions. As an estimate based on the area under the peak, the amount of carbon on the sample treated in the COS-containing gas mixture is less than half of that treated in the sulphur-free gas mixture. In other words, 215 ppb COS has significantly reduced the carbon deposition.

3.3. STEM analysis

3.3.1 Sample treated in the sulphur-free gas mixture

To understand the formation mechanism of nickel-rich particles, FIB was used to extract thin foils from the samples treated in the sulphur-free gas mixture. Figures 6a is an HAADF image showing the typical cross-sectional view of the sample. The region within the rectangular box 'b' was further studied and the chemical composition mapped in Figures 6(b-f). As shown in Figure 6b, the oxide formed above the grain boundary (g.b.) was obviously thinner (of ~100 nm) than that formed over the grain interior (of ~400 nm in Figure 6g). The EDS maps (Figures 6d and 6e) clearly demonstrate that the oxide is a chromium oxide. Above this oxide layer, particles of irregular shape can be observed. The iron and oxygen maps showed that iron oxides were encapsulated by elemental iron forming a core-shell type configuration (see Figures 6c and 6e).

Region ''g' in Figure 6a was studied and chemically mapped in Figures 6(g-k). Features of bright contrast can be observed in the oxide (Figure 6g) and are shown to be nickel-rich (Figure 6k) with some iron (Figure 6h). The gaps in the oxygen (and chromium) map corresponding to these nickel-rich features suggesting that these are not oxides. The composition of these nickel-rich features is characteristic of the particle located at the tip of the filament.

3.3.2. Sample treated in the gas mixture containing 215 ppb COS

Figure 7a is a STEM HAADF image showing the cross-section of the grain centre in a sample treated in the COS-containing gas mixture for 4 hours at 600 °C. The elemental maps (Figures 7c, 7d and 7f) show that an iron-chromium-rich oxide layer of about 100~200 nm thick has formed. Nickel-rich particles were observed (Figure 7e). The nickel-rich particles within the oxide layer are elongated parallel to the metal/oxide interface of typically 20~30 nm thick and can be of ~200 nm long and those above the oxide layer are of irregular shapes of about 50 nm in size.

The chemical information of the nickel-rich particles within the oxide layer was analysed. Figure 8a shows a STEM HAADF image obtained from the sample treated in the COS-containing gas mixture for 4 hours at 600 °C. EDS point analysis of the particle and the surrounding oxide was performed

and the results are shown in Figures 8b and 8c. A small but noticeable sulphur peak exists on the spectrum obtained from the nickel-rich particle (Figure 8b) not on that obtained from the surrounding oxide (Figure 8c).

The EDS elemental maps in Figures 8e and 8f clearly demonstrated that both nickel and sulphur are concentrated on the particle rather than in the oxide. An EDS linescan across the particle is shown in Figures 8g and 8h for nickel and sulphur respectively. The nickel X-ray signal peaks at the centre of the particle, presumably due to the larger thickness of the particle there. It should be noted that the sulphur X-ray signal shows two peaks coincident with the edge of the particle, suggesting that sulphur is not homogeneously distributed within the particle but probably concentrated on the surface of the nickel-rich particle.

3.4. Diffraction analysis

Figure 9a shows a TEM bright field image of a nickel-rich particle of about 50 nm in diameter within the oxide layer of the sample exposed to the COS-containing gas mixture for 4 hours at 600 °C. The electron diffraction patterns obtained from the steel matrix and the particle are shown in Figures 9b and c, respectively. Identical diffraction patterns were acquired from both the steel matrix and the particle. After series tilting experiments, the nickel-rich particle was found to assume the FCC structure and also to have the same crystal orientation as the steel matrix. The diffraction patterns (Figure 10) obtained from a nickel-rich particle and the steel matrix in the sample exposed in the sulphur-free gas mixture for 4 hours also show the same relationship. Figure 11a is a TEM image showing the oxide layer in the sample exposed to the COS-containing gas mixture. The diffraction pattern (Figure 11b) obtained from the grain encircled in pink dashed curves confirmed that the oxide is the FCC structured $FeCr_2O_4$ spinel (chromite).

3.5. Oxide-metal interface

It is well documented [17, 18, 19, 20, 21] that the oxidation of chromium results in the depletion of chromium in the immediate vicinity of the metal/oxide interface. As shown in Figure 12, the chromium depletion is coincident with the nickel enrichment at the metal-oxide interface.

At a further distance from the steel matrix, the oxide is composed of alternating layers containing varying amounts of nickel and chromium. Peaks in nickel showed a corresponding decrease in oxygen. Iron was also present within the oxide but at a more uniform distribution.

Similar nickel enrichment at the oxide-metal interface was also observed in the sample treated in the COS-containing gas mixture, as shown in Figure 13. Figure 13 also shows that a small amount of sulphur was present at the oxide-metal interface. It should be noted that this interfacial sulphur enrichment was only observed at the interface where nickel-enrichment occurred, but not in the oxide nor the steel matrix. No sulphur was observed in the COS-free sample, as expected.

4. Discussion

4.1. Nickel-rich particle formation mechanism

Millward et al [3, 6] observed nickel particle associated with carbon filaments during the oxidation of this steel and based on the fact that the only source of nickel is the steel itself, they suggested that the catalytic nickel nano-particles originated from the alloy during the oxidation process. Under the gas conditions used [3], the oxygen partial pressure was controlled by the CO_2/CO ratio such that nickel was the only alloying element that was thermodynamically stable as a metal with the other alloying elements form oxides.

The results obtained from the current study have confirmed that nickel enriched at the metal-oxide interface where chromium and iron were preferentially oxidised to form chromite. As shown schematically in Figure 14a, as oxidation proceeds, the nickel-enriched regions break up into individual particles and are left in the oxide as the internal oxidation front (oxide-metal interface) moves inward (Figures 14b and 14c). This is consistent with the observation that nickel-rich particles in the oxide sometimes are elongated and parallel to the metal/oxide interface (see for example Figure 7e). During this process, it would be expected that the nickel-rich particles formed maintain the crystallography orientation as that of the metal matrix due to the fact that both are of FCC structure with similar lattice parameters. This was indeed confirmed by the electron diffraction patterns taken

from samples treated in both the COS-free and the COS-containing gases (Figures 9 and 10). In the current work, it seems that the orientation of these nickel-rich particles had not been altered during further oxidation. However, it was noticed that wherever the carbon filaments have been observed, the nickel-rich particles attached have very different orientations with the steel matrix likely due to the attached carbon filaments.

It has been found that, close to grain boundaries, the chromium oxide layer is thin (~100 nm in Figure 6 for example). This is probably due to the fast diffusion along grain boundaries, chromium oxide (chromia) formed at the early stage of the oxidation was dense and slowed down the further oxidation, thus, preventing the formation of nickel enriched region. While away from the grain boundaries, the oxide layer was much thicker and it is $FeCr_2O_4$ (chromite).

In the current study, the thickness of the oxide (chromite) formed in the COS-free gas mixture was approximately 300 ~ 500 nm while that formed in the COS-containing gas mixture of about 100 ~ 200 nm. In other words, the oxidation kinetics in the COS-containing gas is slower. Although the role of sulphur on the oxidation kinetics has not been systematically studied, literature [22, 23] suggested that sulphur has an effect on the initial oxide nucleation. It was suggested that the initial oxidation requires adsorption of an oxygen molecule onto the metal surface, followed by the nucleation of oxide. However, when an alloy is exposed to a sulphur containing gas (such as COS in this case), it is probably that sulphur has a stronger affinity to the metal and adsorbs preferentially onto the surface of the alloy. To initiate the oxide formation, sulphur must first be replaced by oxygen. As a result of the competing surface adsorption, the initial oxidation process is slowed in the presence of sulphur.

4.2. Inhibition mechanism (the distribution of sulphur in the alloy)

In the present work, the filamentary carbon deposition on the sample treated in the sulphur-free gas mixture was shown to be catalysed by nickel-rich particles. Adding 215 ppb of COS to the gas mixture effectively suppressed the carbon deposition. Although nickel-rich particles were also formed during the oxidation in the COS-containing gas mixture, it seems that these particles are no longer catalytic. It was postulated [14] that there are two possible ways by which catalysts can be

deactivated, *viz*. by converting metallic nickel-rich particles to sulphide or by the surface poisoning of nickel-rich particles.

According to the literature [24, 25], the thermodynamically most stable form of nickel sulphide is Ni_3S_2 which assumes a rhombohedral crystal structure [26]. In this study, the diffraction analysis suggests that the sulphur concentrated at the surface of the nickel-rich particles. The nickel-rich particles assume an FCC structure with the lattice parameter of about 0.36 nm, i.e., consistent with that of metallic nickel, but not Ni_3S_2. A thermodynamic calculation showed that about 680 ppb of COS is required to form Ni_3S_2 in equilibrium with 1 % CO at 600°C [27]. In other words, a much higher COS concentration than used in the present tests would be required for Ni_3S_2 to be stable thermodynamically.

Ni_3S_4 is the only nickel sulphide binary phase assuming the FCC structure [28] however with a lattice parameter of 0.9457 nm [29], much larger than the 0.36 nm determined from the nickel-rich particles formed in this study. Therefore, it can be concluded that these nickel-rich particles studied in the current work are not nickel sulphide but metallic nickel-rich particles.

In the sample exposed in the COS-containing gas mixture, sulphur was observed on the surface of nickel-rich particles and also associated with the nickel-enriched region at the metal/oxide interface. Using a Langmuir-Hinshelwood approach, McGurk [27] calculated that at 600 °C, a COS content of 160 ppb in the gas mixture would be sufficient to cover 80% of the surface of nickel-rich particles with sulphur. The 215 ppb of COS used in the present work is thus sufficient to cover the vast majority of the surface of the nickel-rich particles. The observation of sulphur adsorption to the surface of nickel-rich particles is consistent with a number of previous studies [30, 31, 32, 33]. In particular, Bartholomew and Katzer [31] reviewed several studies on the poisoning of nickel catalysts by H_2S in CO hydrogenation and concluded that the formation of surface nickel-sulphur bonds was significantly more favourable than the formation of bulk nickel-sulphur bonds.

5. Conclusions

Exposure to the gas mixture of about 1000 ppm C_2H_4/ 1% CO/ Bal. CO_2 at 600°C resulted in filamentary carbon deposition on the surface of a 20Cr-25Ni stainless steel. The carbon filaments were associated with metallic nickel-rich particles, consistent with literature reports that the carbon deposition was catalysed by these particles. Inhibition of this filamentary carbon deposition was achieved by adding 215 ppb of COS to the gas mixture. The following concluding remarks can be drawn from the electron microscopy studies performed in this work:

1. Nickel-rich metallic particles existed in the samples treated in both COS-free and COS-containing gas mixtures. Electron diffraction experiments confirmed that these nickel-rich particles assumed the same FCC crystal structure and orientation as the steel matrix and the lattice parameter was about 0.36 nm similar to that of the steel matrix. Nickel enrichment at the metal-oxide interface has also been observed. Under the current experiment conditions, both iron and chromium oxidised, leaving nickel enriched at the metal-oxide interface which became detached from the steel matrix with further oxidation. Therefore, these nickel-rich particles maintained the same crystal structure and orientation as that of the underneath steel matrix.
2. STEM-EDS results confirmed that sulphur concentrates on the surface of the nickel-rich particles and also at nickel-enriched regions at the metal-oxide interface. However, no existence of nickel sulphide has been observed. As such surface adsorption of sulphur can be regarded as the reason for the observed suppression of carbon deposition when treated in the COS-containing gas mixture.
3. In the current work, the oxide layer formed was thinner when COS was added than that without COS. This might be caused by the slowed oxide nucleation or the slowed diffusion across the metal-oxide interface when sulphur enriches, due to the strong nickel-sulphur affinity. Further work will be needed to clarify this.

Acknowledgements

The authors would like to thank Dr Jing Wu, Mr Jinsen Tian and Dr Rayan M Ameen for assisting with the electron microscopy. This work was funded partly by EDF Energy and by the Engineering and Physical Sciences Research Council (EPSRC). The project has benefited from the access to facilities funded by EPSRC (EP/L017725/1) and those at the Centre for Electron Microscopy of the University of Birmingham.

Table 1: Alloy Composition, wt.%.

Cr	Ni	Mn	Nb	C	Fe
19.0	26.5	0.67	0.6	0.051	Bal.

Table 2: Composition of the deposition gas as supplied by BOC.

Gas mixture	C_2H_4 ppm	CO %	COS ppb	CO_2
1	1045	0.96	-	bal.
2	1048	0.99	215	bal.

List of Figures

Figure 7: (a) STEM HAADF image showing the cross-section of a sample exposed to the COS-containing gas mixture. (b) A higher magnification STEM image of region 'b' shown in the red box in (a) and the corresponding EDS elemental maps of iron (c), chromium (d), nickel (e) and oxygen (f).

Figure 8: Qualitative EDS analysis of a nickel-rich particle within the oxide layer in the sample that was exposed to the COS-containing gas. (a) STEM image of the particle within the oxide layer. Point EDS confirmed the presence of (b) sulphur in the particle, but not in the oxide (c) where the signal is at the background level. (d) Magnified image of the particle seen in (a). Elemental maps showing the distribution of (e) Ni and (f) S across the particle. (g) Ni and S line-profile across the particle shows that the sulphur is concentrated around the edge of the particle. This implies that sulphur is present on the surface of the nickel-rich particle.

Figure 9: (a) TEM-BF image of a nickel-rich particle and the electron diffraction patterns obtained from (b) the alloy and (c) the nickel-rich feature for the sample exposed to COS-containing gas. It shows that the nickel-rich feature has the same crystal orientation and FCC structure as the alloy. The particle was positioned by the white circle in (a).

Figure 10: (a) TEM-BF image of nickel-rich features and the electron diffraction patterns obtained from (b) the alloy and (c) the nickel-rich feature (in black contrast) for the sample exposed to the COS-free gas mixture. It shows that the nickel-rich feature has the same orientation and FCC structure as the alloy.

Figure 11: (a) A cross-sectional STEM-BF image obtained from a sample exposed to the COS-containing gas mixture. The diffraction pattern (b) taken from the oxide grain in dark contrast (highlighted in pink) is consistent with that of the FCC structured chromite.

Figure 12: (a) and (b) A cross-sectional STEM image of the sample exposed to sulphur-free gas mixtures. The concentration profiles of (c) O, (d) Cr, (e) Fe and (f) Ni across the oxide-metal interface.

Figure 13: (a) STEM image showing the cross-section of the sample exposed to COS-containing gas mixture. The concentration profiles obtained from the linescan across the oxide-metal interface following the yellow line in (a) are shown in (b) Cr, (c) Ni, (d) Fe (e) S and (f) O.

Figure 14. Schematic diagrams of the mechanism leading to the formation of the nickel-rich particles within the oxide at the grain centres.

Data Availability

The raw/processed data required to reproduce these findings cannot be shared at this time due to legal or ethical reasons.

References

[1] A. Dyer, Gas chemistry in nuclear reactors and large industrial plant, London: Heyden, 1980.

[2] T. I. Barry and A. T. Dinsdale, "High temperature corrosion and deposition phenomena on stainless steels," *Materials Science and Technology,* vol. 10, p. 1090, 1994.

[3] G. R. Millward, H. E. Evans, M. Aindow and C. W. Mowforth, "The Influence of Oxide Layers on the Initiation of Carbon Deposition on Stainless Steel," *Oxidation of Metals,* vol. 56, p. 231, 2001.

[4] D. J. Young, J. Zhang, C. Geers and M. Schuetze, "Recent advances in understanding metal dusting: A review," *Materials and Corrosion,* vol. 62, no. 1, p. 7, 2011.

[5] J. Zhang, P. Munroe and D. J. Young, "Microprocesses in nickel accompanying metal dusting," *Acta Materialia,* vol. 56, no. 1, p. 68, 2008.

[6] G. Millward, H. Evans, I. Jones and C. Eley, "Carbon deposition on stainless steel in oxidising environments," *Materials at High Temperatures,* vol. 20, p. 535, 2003.

[7] R. A. Holm and H. E. Evans, "The resistance of 20Cr/25Ni steels to carbon deposition. IV. The influence of alloy silicon content," *Werkstoffe and Korrosion,* vol. 38, p. 224, 1987.

[8] W. Karcher and P. Glaude, "Inhibition of carbon deposition on iron and steel surfaces," *Carbon,* vol. 9, p. 617, 1971.

[9] J. R. Rostrup-Nielsen, "Sulfur-Passivated Nickel Catalysts for Carbon-Free Steam Reforming of Methane," *Journal of Catalysis,* vol. 85, p. 31, 1984.

[10] W. T. Owens, N. M. Rodriguez and R. T. K. Baker, "Effect of Sulphur on the interaction on nickel with ethylene," *Catalysis Today,* vol. 21, p. 3, 1994.

[11] M. S. Kim, N. M. Rodriguez and R. T. K. Baker, "The interplay between sulphur adsorption and carbon decomposition on cobalt catalysts," *Journal of Catalysis,* vol. 143, p. 449, 1993.

[12] C. D. Tan and R. T. K. Baker, "The effect of various sulfides on carbon deposition on nickel-iron particles," *Catalysis Today,* vol. 63, p. 3, 2000.

[13] M. P. Taylor, H. E. Evans, P. J. Smith, R. Ding, Y. L. Chiu, S. Rai, B. J. Connolly, N. Smith, L. Pearson and C. Mowforth, "The Effect of Temperature and Carbonyl Sulphide on Carbon Deposition on 20Cr25Ni Stainless Steel," *Oxidation of Metals,* vol. 87, no. 5-6, p. 667, 2017.

[14] G. R. Millward, H. E. Evans, C. D. Eley and C. W. Mowforth, "The influence of carbonyl sulphide on the inhibition of filamentary carbon deposition on stainless steel," *Materials and corrosion,* vol. 54, p. 864, 2003.

[15] R. A. Holm and H. E. Evans, "The resistance of 20Cr/25Ni steels to carbon deposition. I. The role

of surface grain size.," *Materials and Corrosion,* vol. 38, p. 115, 1987.

[16] C. Park and R. T. K. Baker, "Carbon Deposition on Iron–Nickel during Interaction with Ethylene–Hydrogen Mixtures," *Journal of Catalysis,* vol. 179, no. 2, p. 361, 1998.

[17] C. Wagner, "Theoretical Analysis of the Diffusion Processes Determining the Oxidation Rate of Alloys," *Journal of The Electrochemical Society,* vol. 99, no. 10, p. 369, 1952.

[18] D. P. Whittle, D. J. Evans, D. B. Scully and G. Wood, "Compositional changes in the underlying alloy during the protective oxidation of alloys," *Acta Metallurgica,* vol. 15, no. 9, p. 1421, 1967.

[19] H. E. Evans, D. A. Hilton and R. A. Holm, "Chromium-depleted zones and the oxidation process in stainless steels," *Oxidation of Metals,* vol. 10, no. 3, p. 149, 1976.

[20] J. Barbehon, A. Rahmel and M. Schutze, "Behavior of the Scale on a 9.5Cr Steel under Cyclical," *Oxidation of Metals,* vol. 30, no. 1-2, p. 85, 1988.

[21] J. Vossen, P. Gawenda, K. Rahts, M. Röhrig, M. Schorr and M. Schütze, "Limits of the oxidation resistance of several heat-resistant steels under isothermal and cyclic oxidation as well as under creep in air at 650°C," *Materials at High Temperatures,* vol. 14, no. 4, p. 387, 1997.

[22] H. J. Grabke, R. Dennert and B. Wagemann, "The effect of S, N, and C on the oxidation of Ni-20%Cr and Fe-20%Cr," *Oxidation of Metals,* vol. 47, no. 5, p. 495, 1997.

[23] H. G. Grabke, "Surface and interface segregation in the oxidation of metals," *Surface and Interface Analysis,* vol. 30, p. 112, 2000.

[24] H. GAMSJÄGER, J. BUGAJSKI, T. GAJDA, R. J. LEMIRE and W. PREIS, Chemical Thermodynamics of Nickel, Chemical Thermodynamics Vol. 6, Elsevier, 2005.

[25] A. Vignes, Extractive Metallurgy 1: Basic Thermodynamics and Kinetics, Wiley, 2013.

[26] M. E. Fleet, "The crystal structure of heazlewoodite, and metallic bonds in sulfide minerals," *American Mineralogist,* vol. 62, p. 341, 1977.

[27] J. C. McGurk, "Long Term Variations in Hydrogen Concentration in AGR Gas Circuits," Internal Report, AEA Technology plc, 2002.

[28] H. J. Okamoto, "Ni-S (Nickel-Sulfur)," *Journal of Phase Equilibria and Diffusion,* vol. 30, no. 1, p. 123, 2009.

[29] D. J. Vaughan and J. R. Craig, "The crystal chemistry of iron-nickel thiospinels," *American Mineralogist ,* vol. 70, p. 1036, 1985.

[30] J. R. Rostrup-Nielsen, "Chemisorption of hydrogen sulfide on a supported nickel catalyst," *Journal of Catalysis,* vol. 11, p. 220, 1968.

[31] C. H. Bartholomew and J. R. Katzer, “Sulfur Poisoning of Nickel in CO Hydrogenation,” in *Catalyst Deactivation: Proceedings of the International Symposium*, Antwerp, 1980.

[32] J. G. McCarty and H. Wise, “Thermodynamics of sulfur chemisorption on metals. I.,” *The Journal of Chemical Physics ,* vol. 72, p. 6332, 1980.

[33] J. H. Wang and M. Liu, “Computational study of sulfur–nickel interactions:A new S-Ni phase diagram,” *Electrochemistry Communications,* vol. 9, p. 2212, 2007.

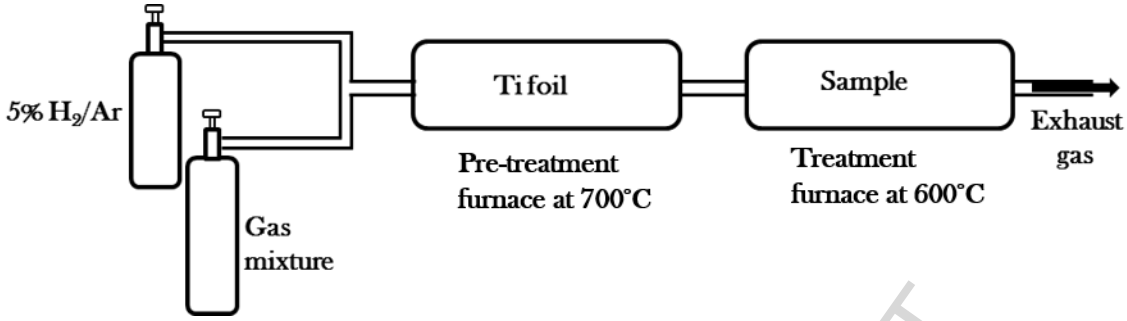

Figure 1: Schematic drawing showing the deposition test rig set-up.

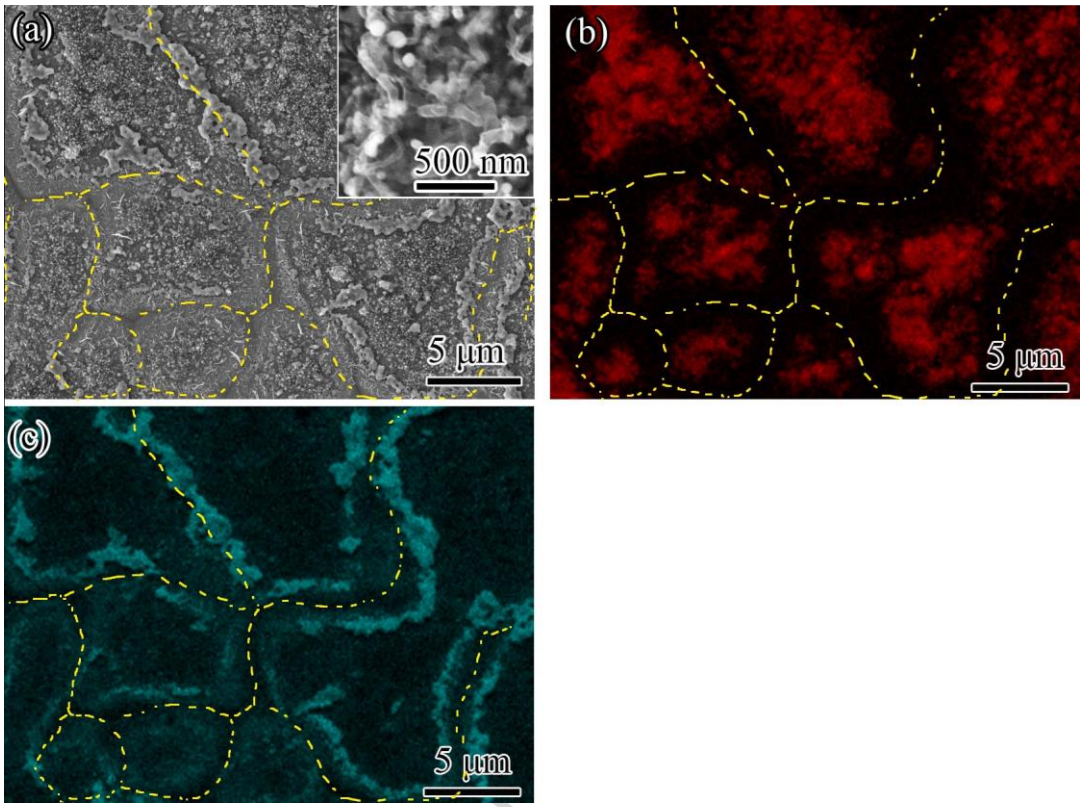

Figure 2: (a) SEM image showing the surface of sample following the 4 hours exposure at 600 °C to the sulphur-free deposition gas mixture. The insert shows a high magnification SEM image of individual carbon filaments. The corresponding EDS elemental map of carbon and iron are shown in Figure 2(b) and Figure 2(c) respectively. Yellow dashed lines outline the grain boundary.

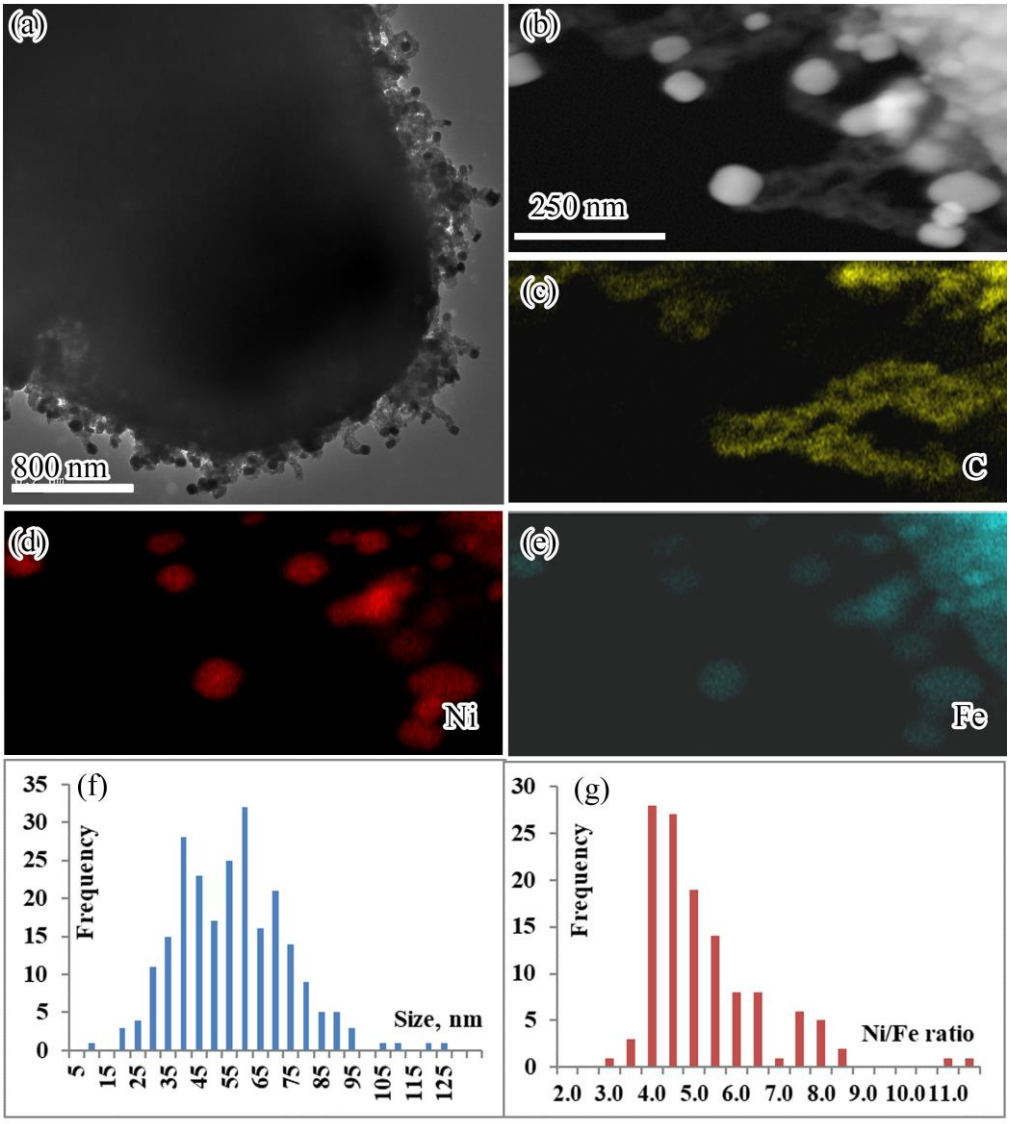

Figure 3: TEM bright field (a) and STEM-HAADF (b) images showing bright small particles are attached to the carbon filaments at the edge of the sample tested in the sulphur-free gas for 4 hours at 600 °C. The particles can be seen at the tip of each filament. Elemental maps of carbon (c), nickel (d) and iron (e) from the same region as in (b). (f) The size distribution and (g) nickel-iron ratio of the particles located at the tip of the filaments.

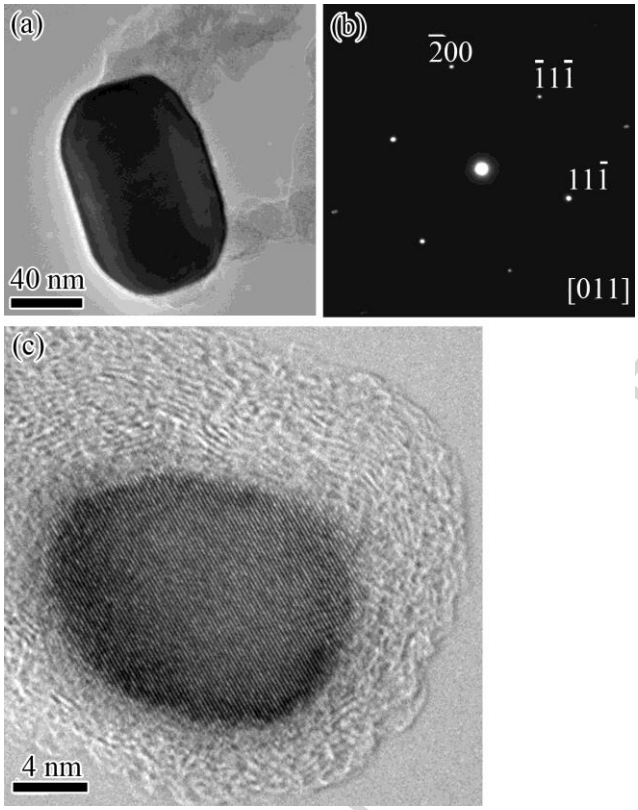

Figure 4:(a) TEM image of a nickel-rich particle obtained from a sample exposed in the sulphur-free gas mixture for 4 hours at 600 °C. Electron diffraction pattern obtained from the particle (b) is consistent with the FCC structure. A high resolution image (c) showing the turbostratic carbon surrounding a nickel rich particle with lattice spacing close to the {111} inter-planar spacing of nickel.

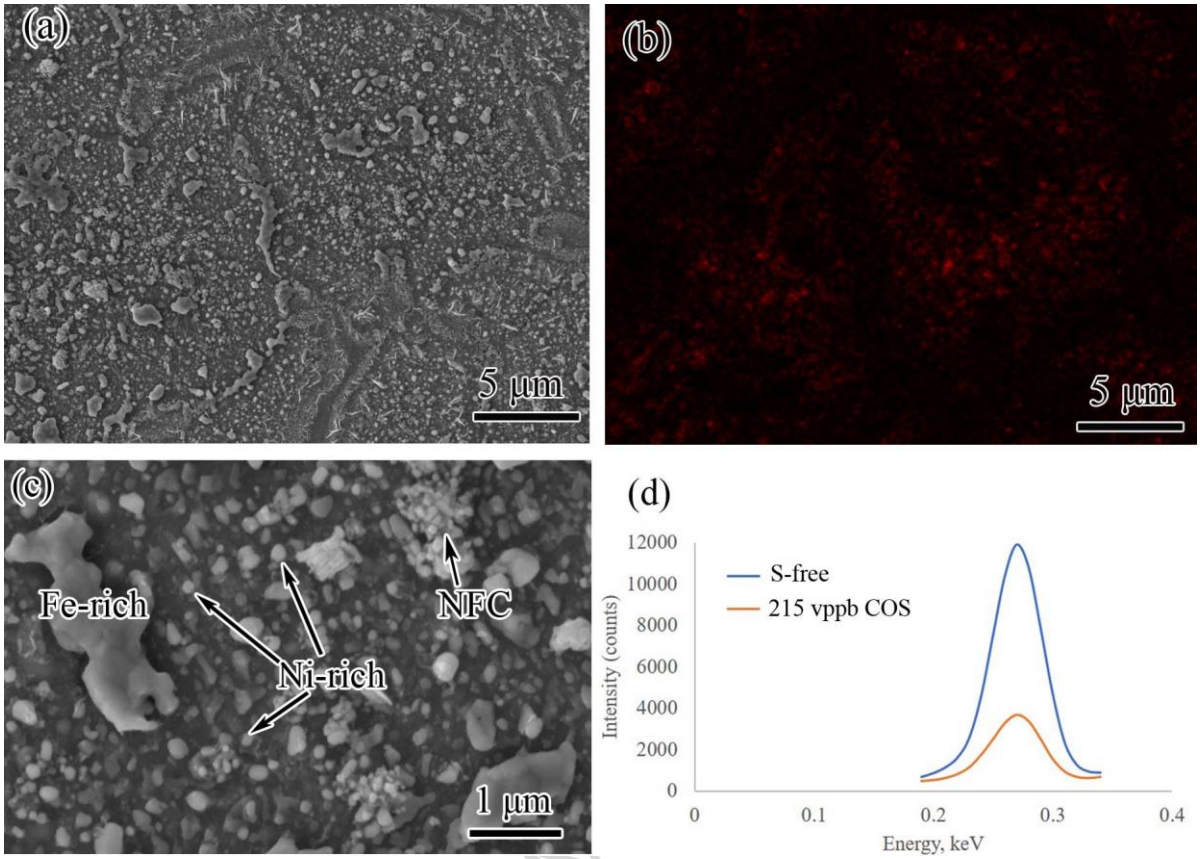

Figure 5: (a) SEM image showing the surface of the sample following the 4 hours exposure to the deposition gas with 215 ppb COS at 600 °C. (b) Elemental carbon map corresponding to (a). (c) Higher magnification SEM image showing the surface covered with scattered nickel- and iron-rich white particles and carbon deposit that glued some nickel-iron rich particles into agglomeration (identified as NFC). (d) EDS carbon X-ray spectra collected from a surface area of 44 µm by 58 µm on both samples under identical electron microscope settings. The total carbon X-ray counts collected from the sulphur-free and COS-containing samples are 71k and 26k, respectively. Clearly, the addition of 215 ppb COS into the gas mixture has resulted in the significant suppression of carbon deposition.

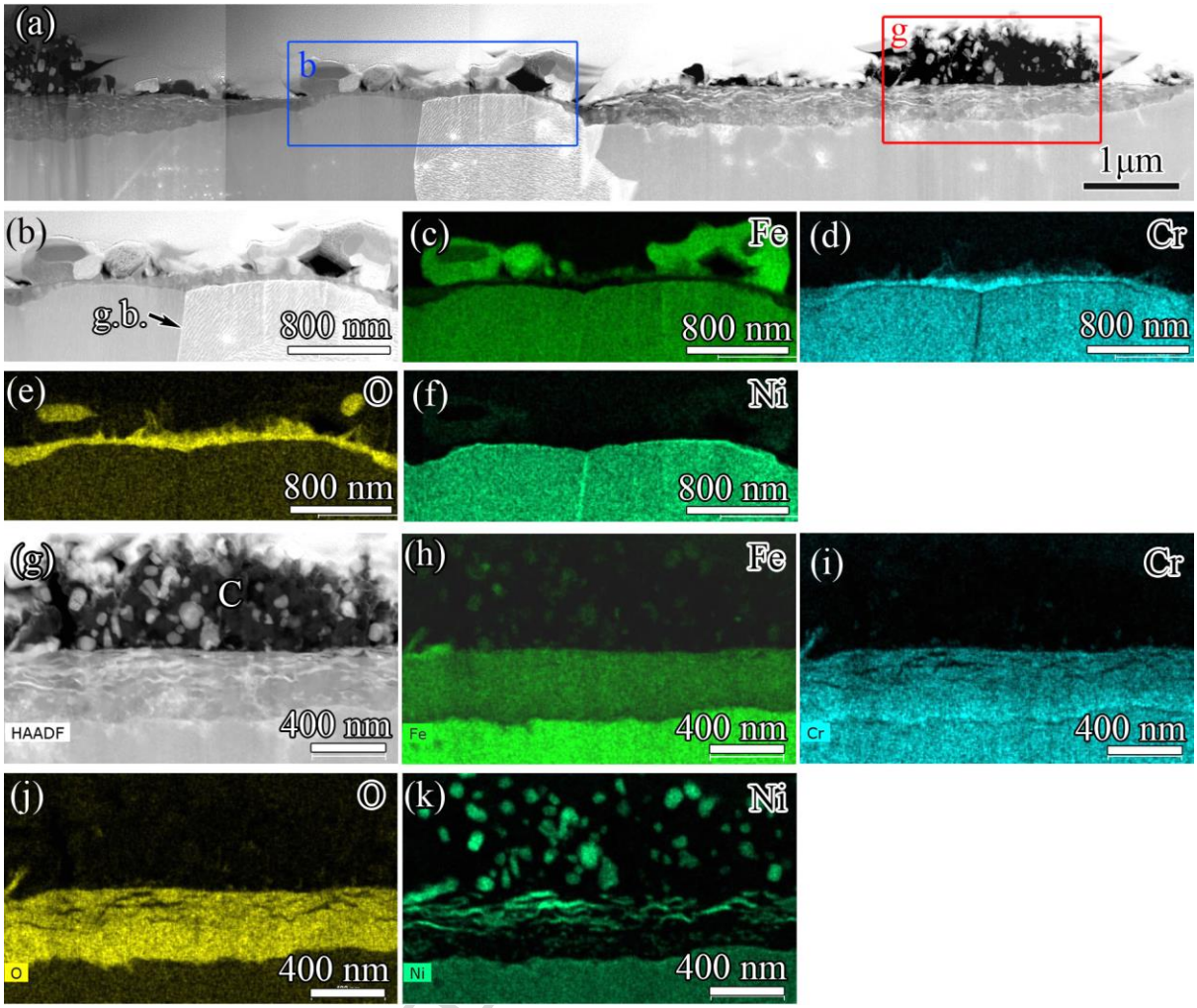

Figure 6: (a) STEM image of a cross-section through the surface of a sample exposed to a sulphur-free deposition gas mixture. Region b (within the blue rectangle) and Region g (within the red rectangle) were mapped and presented in Figures (b-f) and Figures (g-k), respectively. (b) A higher magnification STEM image of the region in the blue box region b. The elemental maps of (c) iron, (d) chromium (e) oxygen and (f) nickel corresponding to (b). (g) STEM image of a cross-section across the grain boundary, shown in the red box in (a). The elemental maps of (h) iron, (i) chromium (j) oxygen and (k) nickel corresponding to (g). EDS maps show the presence of nickel-rich features within the (iron, chromium) oxide layer.

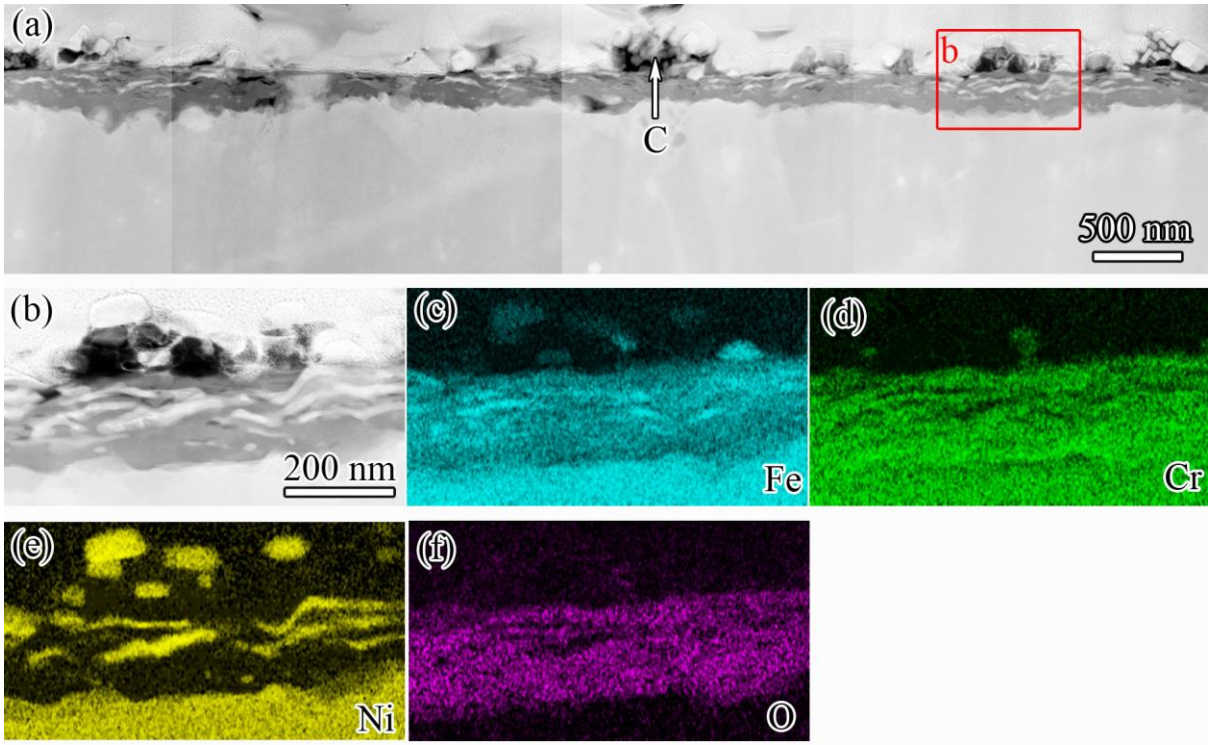

Figure 7: (a) STEM HAADF image showing the cross-section of a sample exposed to the COS-containing gas mixture. (b) A higher magnification STEM image of region 'b' shown in the red box in (a) and the corresponding EDS elemental maps of iron (c), chromium (d), nickel (e) and oxygen (f).

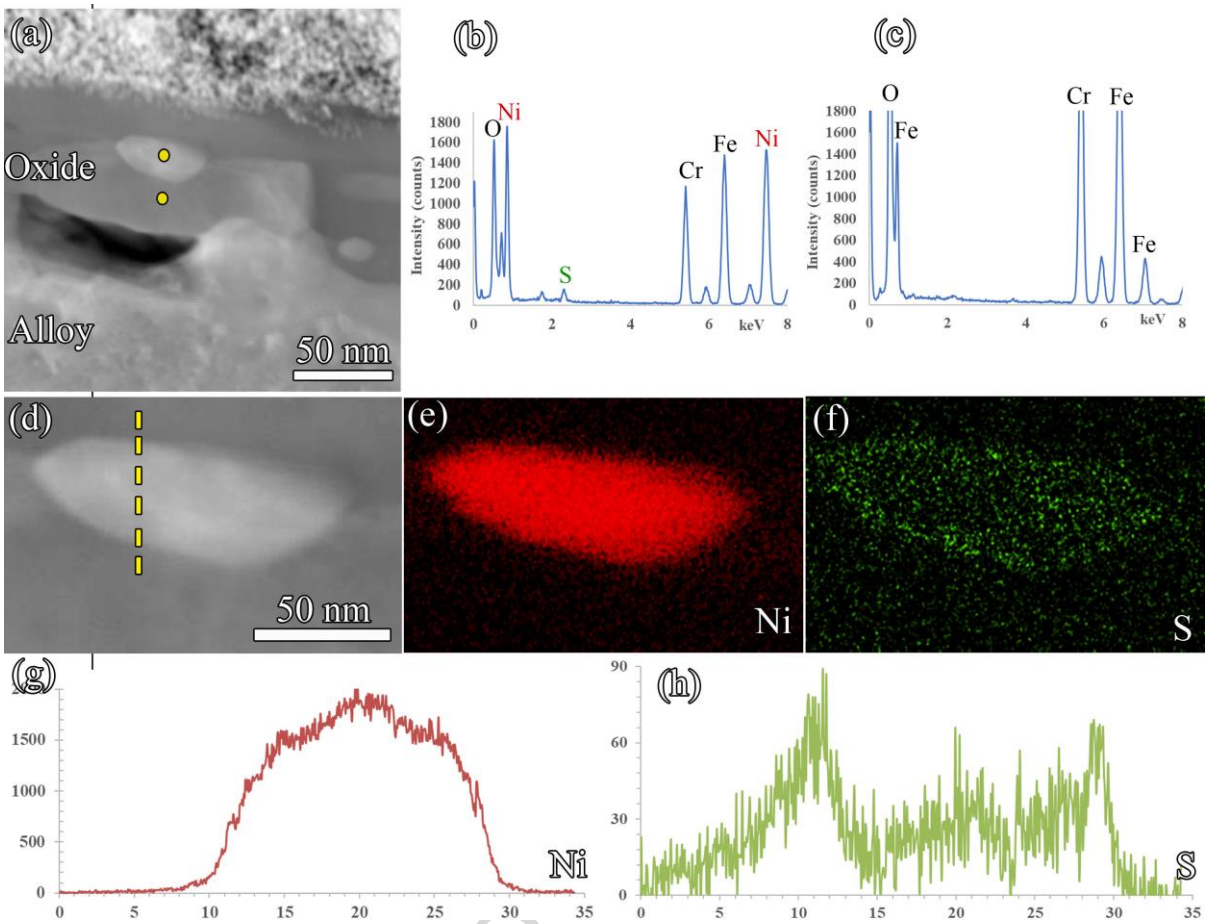

Figure 8: Qualitative EDS analysis of a nickel-rich particle within the oxide layer in the sample that was exposed to the COS-containing gas. (a) STEM image of the particle within the oxide layer. Point EDS confirmed the presence of (b) sulphur in the particle, but not in the oxide (c) where the signal is at the background level. (d) Magnified image of the particle seen in (a). Elemental maps showing the distribution of (e) Ni and (f) S across the particle. (g) Ni and S line-profile across the particle shows that the sulphur is concentrated around the edge of the particle. This implies that sulphur is present on the surface of the nickel-rich particle.

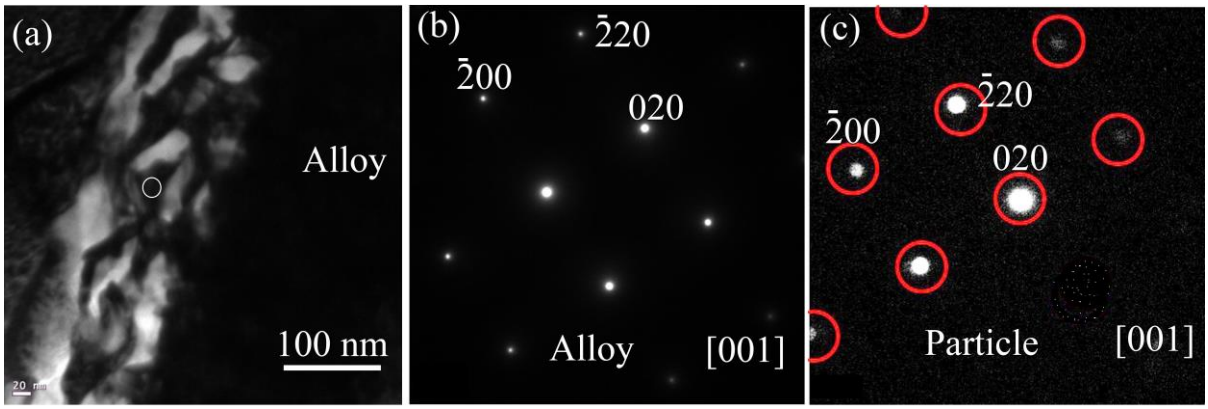

Figure 9: (a) TEM-BF image of a nickel-rich particle and the electron diffraction patterns obtained from (b) the alloy and (c) the nickel-rich feature for the sample exposed to COS-containing gas. It shows that the nickel-rich feature has the same crystal orientation and FCC structure as the alloy. The particle was positioned by the white circle in (a).

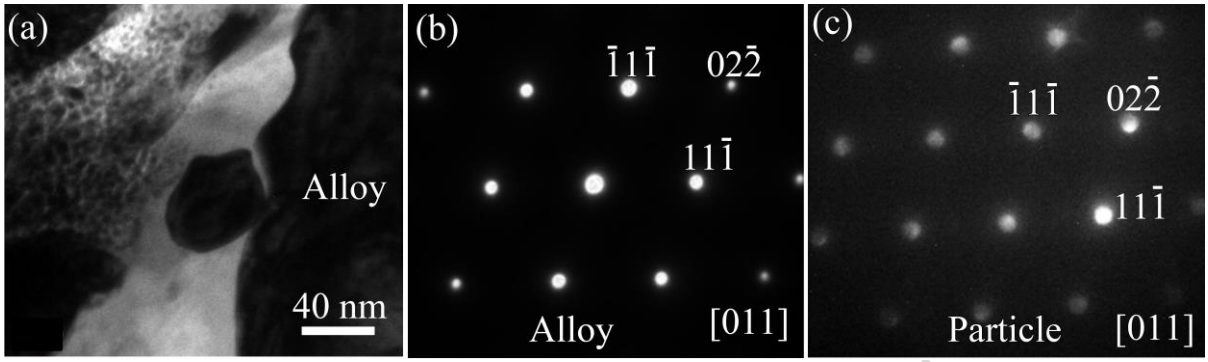

Figure 10: (a) TEM-BF image of nickel-rich features and the electron diffraction patterns obtained from (b) the alloy and (c) the nickel-rich feature (in black contrast) for the sample exposed to the COS-free gas mixture. It shows that the nickel-rich feature has the same orientation and FCC structure as the alloy.

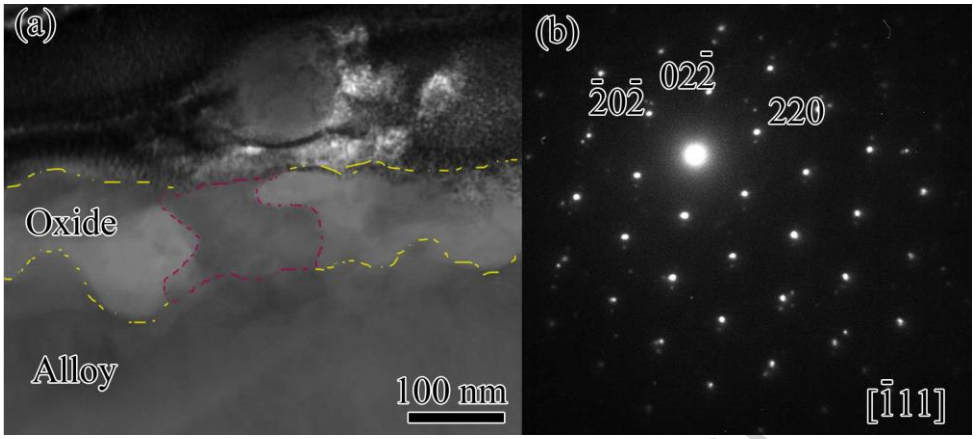

Figure 11: (a) A cross-sectional STEM-BF image obtained from a sample exposed to the COS-containing gas mixture. The diffraction pattern (b) taken from the oxide grain in dark contrast (highlighted in pink) is consistent with that of the FCC structured chromite.

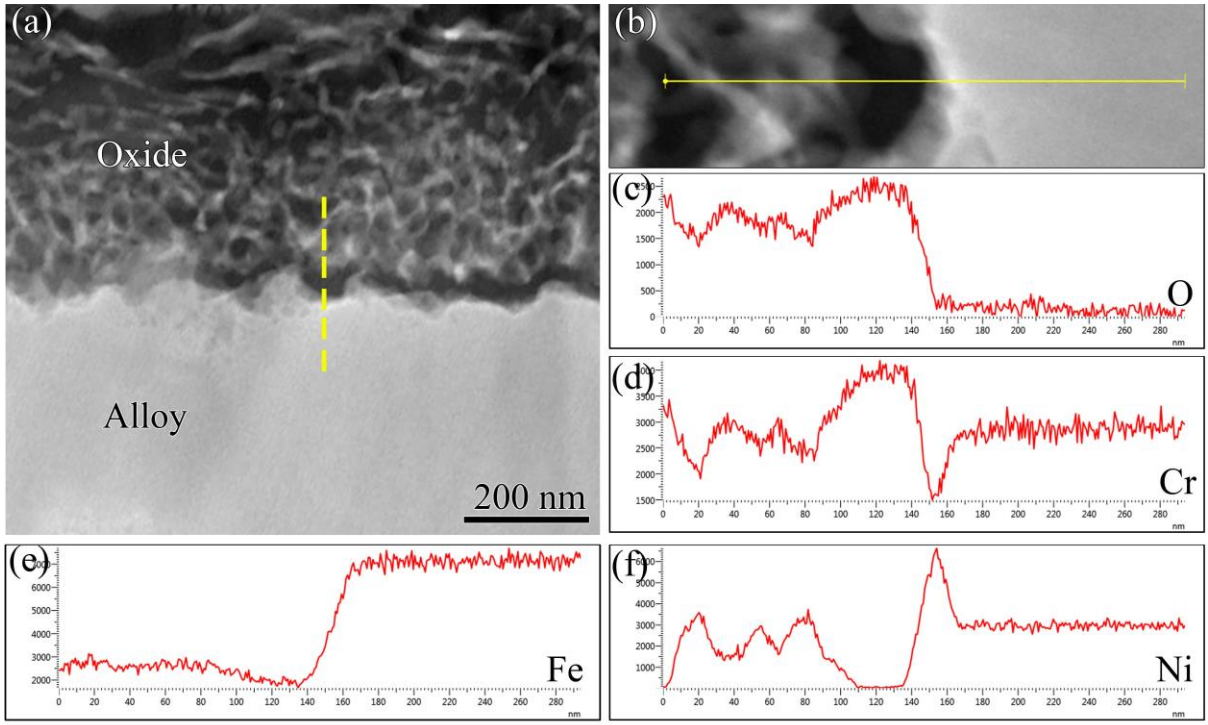

Figure 12: (a) and (b) A cross-sectional STEM image of the sample exposed to sulphur-free gas mixtures. The concentration profiles of (c) O, (d) Cr, (e) Fe and (f) Ni across the oxide-metal interface.

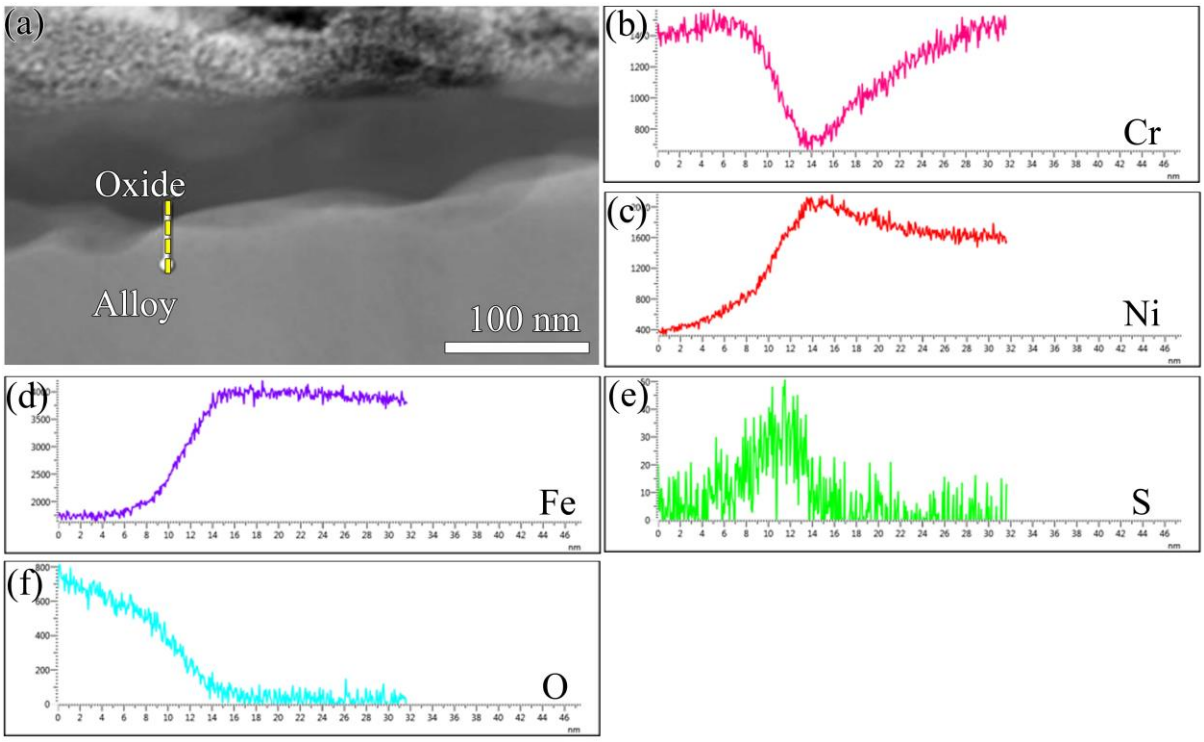

Figure 13: (a) STEM image showing the cross-section of the sample exposed to COS-containing gas mixture. The concentration profiles obtained from the linescan across the oxide-metal interface following the yellow line in (a) are shown in (b) Cr, (c) Ni, (d) Fe (e) S and (f) O.

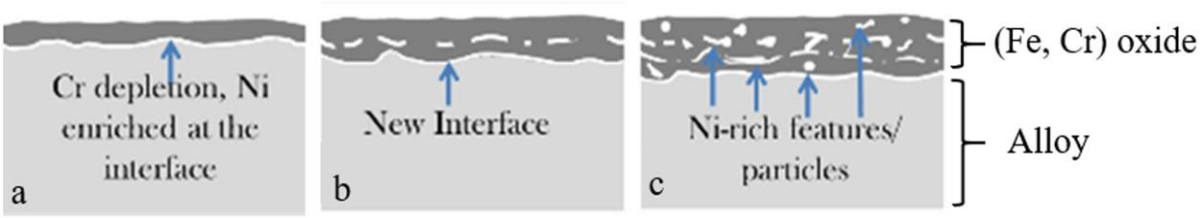

Figure 14. Schematic diagrams of the mechanism leading to the formation of the nickel-rich particles within the oxide at the grain centres.

Highlights

- Carbon deposition has been significantly reduced under the presence of CoS
- The origin of catalytic nickel-rich particles in stainless steel revealed
- High resolution EDS study showed that sulphur was observed to be surrounding nickel-rich particles